Chapter 8: Optimum Design of Small Scale Stand-Alone Hybrid Renewable Energy Systems (by *Dr. Juan M. Lujano-Rojas* from C-MAST, University of Beira Interior – Covilhã, Portugal and INESC-ID, Instituto Superior Técnico, University of Lisbon – Lisbon, Portugal, *Prof. Rodolfo Dufo-López* and *Prof. José L. Bernal-Agustín* from Department of Electrical Engineering, University of Zaragoza – Zaragoza, Spain, *Dr. Gerardo J. Osório* from C-MAST, University of Beira Interior – Covilhã, Portugal, and *Prof. João P. S. Catalão* from C-MAST, University of Beira Interior – Covilhã, Portugal and INESC-ID, Instituto Superior Técnico, University of Lisbon – Lisbon, Portugal, and INESC TEC and Faculty of Engineering of the University of Porto – Porto, Portugal)

Abstract

A crucial factor for the sustainable development of human society is access to electricity. This fact has motivated the development of renewable energy systems isolated or connected to the electric distribution network. Evaluation of autonomous hybrid energy systems from a technical and economic perspective is a difficult problem that requires using complex mathematical models of renewable sources and generators, such as photovoltaic (PV) panels and wind turbines, and the implementation of optimization techniques in order to obtain an economically successful design. This chapter describes and analyzes traditional isolated energy systems powered by solar PV and wind energies provided with a battery energy storage system (BESS). Simulation and optimization are illustrated through the analysis of a rural electrification project in Tangiers (Morocco) in order to provide electricity to rural clinic. Optimization analysis suggests the installation of a PV/BESS system due to the magnitude of the load to be supplied, operating costs, and environmental conditions.

Keywords: Autonomous energy systems, Genetic algorithm, Hybrid power systems, Simulation, Optimization, Lead-acid battery, Stand-alone systems, Degradation, Corrosion, Photovoltaic systems

Chapter contents:

8.1. Introduction

Energy is a leading factor for the development of human beings from a social, cultural and economic perspective. In spite of this, approximately 17% of the world's population still needs an electricity supply [1]; this percentage represents those people who live in rural communities and do not have access to Electric Distribution Network (EDN) or any autonomous energy system. Some problems related to energy provision in remote

areas have an administrative character. An example of this condition is when rural electrification funds are invested; frequently, power resources are assigned so that economically advantaged communities receive the majority of the available economical support.

Other problems arise when those poorest householders are not able to pay the costs related to EDN connection; hence, cost-connection could be considered as a barrier for development of some people living in rural areas. The implementation of a rural electrification program is typically based on two important factors; economical sustainability and welfare. In order to guarantee self-sustained development from an economical perspective, monetary resources are invested according to the distance between the community to be provided with electrical service and the nearest EDN already installed. In addition to this factor, other parameters such as population size and whole community income are taken into account. Another very important factor is the population welfare, which is integrated into the electrification strategy by considering livelihoods, gender role and relationships, and geographical location, among other parameters.

Commonly, all of these features are considered in order to determine the way in which each community is going to be provided with electric service. It could be carried out by using a connection to the nearest EDN, which requires a detailed knowledge about grid-connection costs, or by installing an autonomous Hybrid Power System (HPS), which requires the evaluation of economical-resources allocation by means of subsidies. Electricity can improve people's lifestyle and lead economic growth in a relevant way; it could be used for lighting streets and residential environments, it could be used in public and social facilities such as restaurants, as well as for irrigation. Other important applications are related to the energy supply of household appliances, such as television

and radio, which allows increasing health knowledge about fertility control and other topics.

In addition, health facilities provided with electric service are able to stay open during more time per day [2]. Fig. 8.1 presents the rural electrification rate per region of the world. It is possible to observe that most of the people without access to electricity are located in countries such as sub-Saharan Africa, Southeast Asia, and the rest of developing Asia with 17%, 69%, and 53% of rural electrification rate, respectively [1].

"Insert Fig. 8.1 here"

Recently, several rural electrification projects are being implemented in developing countries such as Cambodia, Bangladesh, and Laos, with 18%, 47%, and 82% of rural electrification rate, in addition to Vanuatu [1]. In Cambodia [3], the efficiency and reliability of EDN has been enhanced by incrementing its capacity and performance at high, medium, and low voltage levels; as a consequence, energy losses of EDN were reduced from 14% to 9.8%. This action had a positive impact on the whole population due to rural energy enterprises, and 565,733 people were provided with a modern energy infrastructure and service. In order to assure the economic sustainability of the electrification project, a regulatory framework for the power sector was designed to improve the commercialization of the service, including its privatization process; as the main results, 297 rural energy enterprises were provided with licenses by the Electricity Authority of Cambodia, and a renewable energy policy was developed so that hydropower generation capacity was increased to 14.5% of the total installed capacity.

An electrification project carried out in Bangladesh [4] allowed the improvement of the population's lifestyle and system performance. Specifically, the rehabilitation of 11,295 km of lines of EDN, joined with the connection of 656,802 new users and the installation of about 3 million Solar Home Systems (SHSs), reduced system losses to

13.7% and reduced illiteracy rates from 21% to 14% by increasing the number of years of continuous scholar activity in school from 6.43 to 6.86 years. Moreover, television improved the lifestyle of women because they got useful information about reproductive health and family planning, among other topics. In Laos [5], rural electrification rate improved 16% as a result of enhancing energy efficiency and renewable energy integration in a substantial form, combined with an increment on the connections to EDN and HPSs installation in remote zones. According to recent information [6], about 42,300 rural households have been electrified by May of 2015, while losses at EDN have been reduced to 13.5% in 2014, in addition to the installation of hydro and biogas units with 50 kW and 260 kW, respectively. In Peru [7], it is estimated that around 105,000 households and small-scale businesses, including around 35,000 indigenous people and 2,900 schools, health clinics and community centers, are going to benefit from a rural electrification project carried out to extend EDN and to incorporate renewable power generation in order to increase access to electric service. Within this group, around 7,100 households will be supplied by using SHSs. In Vanuatu [8], there is a project to supply households, aid posts and community halls in rural areas at which it is not expected that EDN will be extended or any mini-grid will be installed; it is estimated that around 85% of the 20,470 households will benefit from the installation of SHSs.

In this context, simulation and optimal sizing of HPS became a relevant topic of research by many scientific organizations all over the world, supported in many cases by governmental institutions; from this effort, several computational tools have been created:

- Hybrid Optimization Model for Electric Renewables (HOMER) is a simulation and optimization model developed by National Renewable Energy Laboratory

(NREL) of the United States for the analysis of isolated and grid-connected HPS. It is able to consider several power sources for isolated systems and modern electrical grids such as biomass, small-scale hydropower, combined heat and power generation, thermal and electrical loads, real-time and time of use pricing schemes, as well as hydrogen energy storage [9]. The optimization technique used by HOMER consists of the evaluation of all possible combinations of HPS components in order to reduce Net Present Cost (NPC), which could be a time-consuming task depending on the amount of elements considered. To reduce the computational complexity of the problem, HOMER Optimizer® was recently introduced as an optimization tool to be jointly used with HOMER.

- Hybrid2 is a simulation model developed by Renewable Energy Research Laboratory (RERL) of University of Massachusetts (UMass) and NREL. This model is able to provide a reliable simulation of HPS with diesel generators, wind turbines, Photovoltaic (PV) generators with Maximum Power Point Tracker (MPPT), power converter, and electrical loads managed by means of supervisory control to implement optimal management strategies. Time series analysis is used to predict system behavior on a long-term basis, while a probabilistic approach is included at each time step to consider the influence of short-term fluctuations related to renewable generation and load demand [10].
- Improved Hybrid Optimization by Genetic Algorithm (iHOGA) is a simulation and optimization model of isolated and on-grid HPS by means of Genetic Algorithm (GA), which allows obtaining a near-optimal solution in a reasonable computational time, useful when complex systems need to be analyzed. It is able to carry out optimization analysis minimizing NPC (mono-objective

optimization) or minimizing NPC and Greenhouse Gas (GHG) emissions simultaneously (multi-objective optimization). The mathematical model of Battery Energy Storage System (BESS) includes aging mechanisms such as corrosion and degradation phenomena in order to reasonably predict battery bank lifetime; control strategies among other parameters can be optimized, too [11].

- Integrated Simulation Environment Language (INSEL) is a programming language designed by University of Oldenburg (UniOldenburg) to face computational simulation problems in a general sense. It is provided with validated simulation models suitable for renewable energy applications such as solar irradiance simulation and the evaluation of PV and solar thermal generators [12].
- In a similar way, Transient Energy System Simulation Program (TRNSYS) is a software environment able to simulate electrical and thermal systems, as well as traffic flow and biological processes. It is composed of two parts: one part is used to read and evaluate the input data and carry out the computational calculations in order to determine mathematical convergence and thermo-physical behavior, while the another part is used to store the characteristics of each element (pumps, wind turbines, electrolyzers, etc.) in a library [13].

In this chapter, simulation and optimization of small-scale HPSs is illustrated and analyzed. In section 8.2, HPS modeling on an hourly basis is described by including several elements such as PV panels, wind turbines, BESS, power converter, and charge controller. In section 8.3, the methodology for optimal sizing of HPSs by GA is described. In section 8.4, a rural electrification project in Tangiers (Morocco) is carried

out in order to supply a small-rural clinic with electric service. Finally, conclusions and remarks are presented in section 8.5.

8.2. Hybrid Energy Systems Modeling

In a general sense, there is a wide range of components and power sources that could be integrated in a HPS. In many cases, the components to be installed are selected by considering techno-economic parameters, so that PV/Wind/BESS and PV/Diesel/BESS are frequently chosen [14]. Fig. 8.2 presents the typical configuration of a HPS to be installed in a remote area; it is powered by wind and solar energies through a small-capacity wind turbine and a PV generator with a MPPT. An important element is BESS; in most cases this is based on lead-acid batteries with a charge controller to protect the battery bank against extreme operating conditions (for example, by avoiding State of Charge (SOC) values lower than SOC_{min} and controlling the charging process). Power inverter converts energy obtained from the renewable sources and BESS in Direct Current (DC) to Alternant Current (AC) in order to be consumed by the householder. Dump load is an auxiliary energy consumption installed to maintain power balance by dissipating excess of energy produced.

"Insert Fig. 8.2 here"

Typically, a conventional diesel generator is included in order to have a controllable and dispatchable power source; however, costs related to the operation and fuel consumption of these units are high and fuel is difficult to be transported towards isolated zones.

The economic viability of installing a diesel generator strongly depends on the expected number of hours of operation, which is determined by the meteorological conditions and available renewable resources; if the running time is low, then adoption of diesel

generation could be economically viable [15]. A mathematical model of each device is described in the next sub-sections.

8.2.1 Photovoltaic Panel Modeling

In a general sense, power production of a PV panel could be estimated by using (8.1) and (8.2); however, in many cases information provided by the manufacturers is estimated under Standard Test Conditions (STC), so that power generation under actual conditions could be approximated by using this information. STC are defined for a solar radiation of 1 kW/m^2 and cell temperature of 25 °C without wind; then, evaluating PV power for STC and actual conditions through (8.1) and (8.2), and combining these expressions, PV power in terms of actual solar radiation and cell temperature is obtained (equations (8.3) and (8.4)) [16,17].

$$P_{pv(t)} = A_{pv} G_{(t)} \eta_{pv(t)} \tag{8.1}$$

$$\eta_{pv(t)} = \eta_{STC}\left[1 + \alpha\left(T_{c(t)} - 25\ °\text{C}\right)\right] \tag{8.2}$$

$$P_{pv(t)} = P_{STC}\left\{\left(\frac{G_{(t)}}{1\ \text{kW/m}^2}\right)\left[1 + \alpha\left(T_{c(t11)} - 25\ °\text{C}\right)\right]\right\} \tag{8.3}$$

$$T_{c(t)} = T_{a(t)} + \left(\frac{T_{NOCT} - 20\ °\text{C}}{0.8\ \text{kW/m}^2}\right) G_{(t)} \tag{8.4}$$

Incorporation of MPPT allows extracting maximum available power from the PV generator according to the current meteorological conditions by modifying the voltage at the terminals; hence, voltage effects on PV performance could be partially avoided in the mathematical formulation [16].

8.2.2 Wind Turbine Modeling

Energy contained in the wind is transformed into electricity through the wind turbine. Fig. 8.3 shows a general purpose power curve of a small-capacity wind turbine typically used in HPS. As can be observed, a wind speed value between 3 and 4 m/s is enough to produce power; this wind speed value is known as cut-in speed. Then, as wind speed rises, frequently to a value between 12 and 15 m/s, power generation increases until the

rated power of the wind turbine (P_w^r); wind speed at this stage is known as the rated wind speed. Finally, when wind speed increases to 18 m/s approximately, output power is reduced to a range between 30% and 70% of the rated power in order to protect the turbine structure [15, 16].

"Insert Fig. 8.3 here"

8.2.3 Battery Energy Storage System Modeling

BESS has been widely analyzed in the technical literature and as a result, several mathematical models were developed to describe its performance. Shepherd [18] developed a mathematical model to describe charging and discharging behavior in terms of open-circuit voltage and its variation with SOC through a linear relation, as well as the variation of battery voltage at its terminals. Manwell and McGowan [19] developed Kinetic Battery Model (KiBaM) inspired on the chemical kinetics; this model assumes that energy could be stored on the battery to be instantly affordable or limited by the chemical reaction. An important advantage of this model is that it is suitable to be used on simulation analysis on an hourly basis and only requires the determination of three parameters.

Copetti *et al.* [20] carried out an extensive experimental work in order to analyze the behavior of internal resistance for charging and discharging processes under several current rates and ambient temperature values. From this effort, a normalized mathematical model was developed based on the assumption that the product between the resistance and the capacity remains constant from one battery to another one. Guash and Silvestre [21] extended the model presented in [20] by incorporating several concepts such as Level of Energy (LOE) and State of Health (SOH), in addition to considering behavior of the battery as a sequence of steady states such as saturation,

overcharge, charge, discharge, and over-discharge or exhaustion, avoiding the analysis of transient phenomena.

Regarding BESS lifetime, Svoboda *et al.* [22] defined operating categories for BESS based on stress factors frequently used by HPS experts. Using the charge factor, *Ah* throughput, highest discharge rate, time between full charge, time at low SOC, and partial cycling as stress factors, and analyzing aging mechanisms related to grid corrosion, active mass degradation, active mass shedding, hard-irreversible sulphation of active mass, water loss-drying out, and electrolyte stratification, several categories were identified. The corresponding categories consider several HPS operating conditions from systems with deficient power generation with deep and shallow cycle operation, BESS with shallow cycling combined with overcharge, deep cycling operation combined with strong charges, BESS with limited charges, as well as BESS under optimal operating conditions from a qualitative point of view. All these categories could be used to help HPS designers to evaluate BESS behavior.

Schiffer *et al.* [23] developed a model at which *Ah* throughput over battery lifetime is weighted according to the operating conditions. This approach is known as weighted *Ah* throughput method. The values of weighting factors are assigned according to Depth of Discharge (DOD), current rate, acid stratification, and time since the last full charging; this method is a heuristic way to represent aging mechanisms of lead-acid batteries. Dufo-López *et al.* [24] carried out a comparative analysis between weighted *Ah* throughput method and real-life data, finding an estimation error between 6.5% and 13.7%. Due to the important capabilities of the last described model to simultaneously include BESS performance and aging models, the proposed work used it in this chapter in order to illustrate BESS behavior in a typical HPS; in general sense, this is an aging

model with medium mathematical complexity that allows optimizing the operating strategy and conditions of BESS with a computational difficulty of a medium level [25]. This model is composed of two main parts: performance analysis and aging mechanisms evaluation. During performance analysis, battery voltage and SOC are determined for a single cell, including the effects of charge controller and the other components of HPS. This process is carried out by using the Shepherd model, in which SOC is estimated taking into account the effects of gassing; then, aging mechanisms (corrosion, acid stratification, sulphation and sulfate crystal growth, and degradation of active material) are analyzed in order to determine lost capacity [23]. In the next sub-sections, all of these processes are briefly described and discussed.

8.2.3.1 Performance model of a typical lead-acid battery

As stated before, battery voltage at each time step is determined by means of the Shepherd model; mathematical expressions for charging ($I_{b(t)} > 0$) and discharging ($I_{b(t)} < 0$) processes are presented in (8.5) and (8.6), where the first term represents the open-circuit voltage under fully charged conditions and constant density of the electrolyte, the second term represents the variations of the open-circuit voltage with DOD, the third term represents the effects of internal resistance, and the fourth term represents operating conditions when the battery is almost fully charged or fully discharged [23, 26, 27].

$$V_{b(t)} = V_0 - gDOD_{(t)} + \rho_{c(t)}\left(\frac{I_{b(t)}}{C_N}\right) + \rho_{c(t)} M_c \left(\frac{I_{b(t)}}{C_N}\right)\left(\frac{SOC_{(t)}}{C_c - SOC_{(t)}}\right);\ I_{b(t)} > 0 \tag{8.5}$$

$$V_{b(t)} = V_0 - gDOD_{(t)} + \rho_{d(t)}\left(\frac{I_{b(t)}}{C_N}\right) + \rho_{d(t)} M_d \left(\frac{I_{b(t)}}{C_N}\right)\left(\frac{DOD_{(t)}}{C_{d(t)} - DOD_{(t)}}\right);\ I_{b(t)} \leq 0 \tag{8.6}$$

SOC is estimated according to (8.7) and (8.8), where the energy effectively stored on the battery is calculated by subtracting the current required by the gassing process related to the hydrogen and oxygen production at the negative and positive electrodes, respectively [23].

$$SOC_{(t)} = SOC_{(t-\Delta t)} + \int_{t-\Delta t}^{t} \left(\frac{I_{b(\tau)} - I^{G}_{b(\tau)}}{C_N} \right) d\tau \tag{8.7}$$

$$I^{G}_{b(t)} = \left(\frac{C_N}{100} \right) \bar{I}^{G}_{b(0)} \left\{ exp\left(c_u \left(V_{b(t)} - \bar{V}^{G}_{b} \right) + c_T \left(T_{a(t)} - \bar{T}^{G}_{N} \right) \right) \right\} \tag{8.8}$$

8.2.3.2 Aging model of a typical lead-acid battery

Corrosion as an aging factor is evaluated by means of the estimation of corrosion voltage of the positive electrode using the Shepherd model, which is presented in (8.9) and (8.10). In a similar way, the first term corresponds to the corrosion voltage under fully charged conditions, the second term corresponds to the influence of DOD, the third term corresponds to the impact of internal resistance, and the fourth term corresponds to the operating conditions when the battery is almost fully charged or fully discharged.

However, in this formulation, DOD impact has been weighted with the factor 10/13 due to the voltage change between the positive and negative electrodes, while the impact of internal resistance and the current rate was assumed to be equally distributed [23,27].

$$\begin{aligned} V_{c(t)} = V_0^c - \frac{10}{13} g DOD_{(t)} + \frac{1}{2} \rho_{c(t)} \left(\frac{I_{b(t)}}{C_N} \right) \\ + \frac{1}{2} \rho_{c(t)} M_c \left(\frac{I_{b(t)}}{C_N} \right) \left(\frac{SOC_{(t)}}{C_c - SOC_{(t)}} \right);\ I_{b(t)} > 0 \end{aligned} \tag{8.9}$$

$$\begin{aligned} V_{c(t)} = V_0^c - \frac{10}{13} g DOD_{(t)} + \frac{1}{2} \rho_{d(t)} \left(\frac{I_{b(t)}}{C_N} \right) \\ + \frac{1}{2} \rho_{d(t)} M_d \left(\frac{I_{b(t)}}{C_N} \right) \left(\frac{DOD_{(t)}}{C_{d(t)} - DOD_{(t)}} \right);\ I_{b(t)} \leq 0 \end{aligned} \tag{8.10}$$

Evolution of the corrosion process is represented by the increment of the effective layer thickness ($\Delta W_{(t)}$). This is estimated by means of (8.11) and (8.12); it depends on the

corrosion voltage and the corrosion speed, which is described according to the Lander corrosion speed vs. voltage curve [28] and Arrhenius law [23, 26, 27].

$$\Delta W_{(t)} = \begin{cases} k_s x^{0.6}; x = \left(\frac{\Delta W_{(t-\Delta t)}}{k_s}\right)^{1/0.6} + \Delta t;\ V_{c(t)} < 1.74 \\ \Delta W_{(t-\Delta t)} + k_s \Delta t;\ V_{c(t)} \geq 1.74 \end{cases} \tag{8.11}$$

$$k_s\left(V_{c(t)}, T_{a(t)}\right) = k\left(V_{c(t)}\right) exp\left(k_{s,T}\left(T_{a(t)} - \bar{T}_N^C\right)\right) \tag{8.12}$$

The increment on the internal resistance due to corrosion is estimated by using (8.13)-(8.15), where the limit values of resistance (ρ_{lim}) and capacity loss (C_{lim}^c) are calculated under the assumption that 20% of battery capacity is reduced due to the increment on the internal resistance and 80% is reduced due to loss of active material due to corrosion.

$$\Delta\rho_{(t)} = \rho_{lim}\left(\frac{\Delta W_{(t)}}{\Delta W_{lim}}\right) \tag{8.13}$$

$$\Delta C_{(t)}^c = C_{lim}^c\left(\frac{\Delta W_{(t)}}{\Delta W_{lim}}\right) \tag{8.14}$$

$$\Delta W_{lim} = T\left(L_{flt}\right)\left(k_s^{lim}\right) \tag{8.15}$$

Battery lifetime is estimated at each time instant by using the weighted number of cycles according to (8.16), at which the impact of SOC, current rate, and acid stratification are taken into account; in other words *Ah* throughputs are weighted according to the operating conditions at each time step.

$$Z_{W(t)} = \frac{1}{C_N}\int_0^t I_{b(\tau)}^d f_{(\tau)}^{SOC} f_{(\tau)}^{ACD}\, d\tau \tag{8.16}$$

Lost capacity due to degradation process is estimated by means of (8.17), assuming that battery capacity is 80% of its nominal value at the end of its lifetime [23, 26, 27].

$$\Delta C_{(t)}^d = C_{lim}^d \exp\left(-c_Z\left(1 - \frac{Z_{W(t)}}{1.6 z_{IEC}}\right)\right) \tag{8.17}$$

The effects of operation at a low SOC during a long time since the last full charge ($t - t_0$), as well as the influence of poor charge periods (n) (equation 8.19) and the impact of current rate at the beginning of cycling period (current factor), are combined in the state of charge weighting factor at each time instant ($f_{(t)}^{SOC}$) defined in (8.18). In this way, effects of mechanical stress on the active material due to the operation at low SOC and the increment in the size of sulfate crystals are both integrated [23, 26, 27].

$$f_{(t)}^{SOC} = 1 + \left(c_{SOCo} + c_{SOCmin}\left[1 - min\left(SOC_{(\tau)}\right), \tau \in [t_0, t]\right]\right) \times \sqrt{\frac{I_b^r}{I_{b(t)}}} \sqrt[3]{exp\left(\frac{n}{3.6}\right)} (t - t_0) \tag{8.18}$$

$$n \leftarrow n + \begin{cases} \dfrac{0.0025 - (0.95 - SOC_{max})^2}{0.0025}; & SOC_{max} > 0.9 \\ 0; & SOC_{max} \leq 0.9 \end{cases} \tag{8.19}$$

Total impact of acid stratification at each time step is quantified by means of the factor ($f_{(t)}^{ACD}$) in (8.20), where effective increment of acid stratification and current factor are taken into account.

$$f_{(t)}^{ACD} = 1 + f_{(t)}^{STR} \sqrt{\frac{I_b^r}{I_{b(t)}}} \tag{8.20}$$

Effective increment of acid stratification is represented in (8.21), which is determined by the subtraction between those factors that increases and reduces acid stratification numerically integrated during each time step. On one hand, increment in acid stratification is related to the operation at low SOC and the current factor, which strongly depends on the discharging current at the beginning of cycling period; these phenomena are represented in (8.22). On the other hand, acid stratification is reduced by means of gassing and diffusion processes as expressed in (8.23)-(8.25) [23, 26, 27].

$$f_{(t)}^{STR} = f_{(t)}^{STR} + \int_{t-\Delta t}^{t} \left(f_{(\tau)}^{PLS} - f_{(\tau)}^{MIN}\right) d\tau \tag{8.21}$$

$$f_{(t)}^{PLS} = c_{pls}\left(1 - min\left(SOC_{(t)}\right), \tau \in [t_0, t]\right) exp\left(-3 f_{(t)}^{STR}\right) \frac{I_{b(t)}^{d}}{I_b^r} \quad (8.22)$$

$$f_{(t)}^{MIN} = f_{(t)}^{MIN,G} + f_{(t)}^{MIN,D} \quad (8.23)$$

$$f_{(t)}^{MIN,G} = c_{min} \sqrt{\frac{100}{C_N}} \frac{\bar{I}_{b(t)}^{G}}{\bar{I}_{b(0)}^{G}} exp\left(c_u\left(V_{b(t)} - V_b^r\right) + c_T\left(T_{a(t)} - \bar{T}_N^G\right)\right) \quad (8.24)$$

$$f_{(t)}^{MIN,D} = \frac{8D}{z^2} f_{(t-\Delta t)}^{STR} 2^{\left(T_{a(t)} - 20\ ^\circ\mathrm{C}\right)/10\ \mathrm{K}} \quad (8.25)$$

Variations of effective resistance over battery lifetime for charging and discharging conditions are estimated according to (8.26) and (8.27) and specifically related to the corrosion process.

$$\rho_{c(t)} = \rho_{c(0)} + \Delta\rho_{(t)} \quad (8.26)$$

$$\rho_{d(t)} = \rho_{d(0)} + \Delta\rho_{(t)} \quad (8.27)$$

Finally, actual battery capacity at each time step is calculated by subtracting the capacity lost due to corrosion and degradation from its nominal normalized value, as presented in (8.28), so that when $C_{d(t)}$ reached 80% or an immediately lower value, it is considered that the battery lifetime has been fulfilled [23, 26, 27].

$$C_{d(t)} = C_{d(0)} - \Delta C_{(t)}^{c} - \Delta C_{(t)}^{d} \quad (8.28)$$

8.2.4 Charge Controller

Generally speaking, algorithms for charge control are based on the implementation of three or four stages, depending on the application, which allows optimizing the charge acceptation of the battery and its lifetime. The three-stage algorithm is composed of bulk, absorption, and float charging steps; during bulk charge, the battery is partially-charged until a SOC value between 50% and 80%. In this stage charging current remains constant, while battery voltage increases to a determined value (V_{abs}).

Then, the absorption charge is applied by keeping the battery voltage constant for a determined time interval (t_{abs}), while the charging current is rapidly reduced. At the end of this stage, SOC frequently reaches a value higher than 95%. Finally, during the

float stage, battery voltage is reduced to a determined value (V_{flt}). The four-stage algorithm is composed of bulk and absorption charging stages, followed by an additional step known as equalization charge, carried out in order to increase SOC above 95% by raising the charging voltage until a save limit (V_{eql}) in order to recharge the last 5% in a reduced time (t_{eql}) [29].

The equalization charge allows controlling gassing process in order to diffuse the layers of differing acid density, so that the variations on voltage and current within the battery are minimized [30]. After this stage, the float charge is applied as previously explained. Nowadays, these charging stages are implemented through a feedback control system based on Pulse Width Modulation (PWM) technique in order to control charging current [31]. Fig. 8.4 presents the analysis of a 2V-cell with C_N=1,000 Ah, where the operation of a four-stage controller is described and control variables such as battery voltage, SOC, and charging current are shown.

As can be observed, absorption charge is applied when battery voltage reaches 2.4V (V_{abs}=2.4V), while SOC reaches 90% approximately. Then, the equalization charge is applied by increasing battery voltage until 2.45V (V_{eql}=2.45V); finally, the float charge is applied by reducing battery voltage until 2.25V (V_{flt}=2.25V); hence, the battery is fully charged at the end of the process.

"Insert Fig. 8.4 here"

8.2.5 Power Converter

In many simulation models presented in the literature, the power converter is represented by means of a constant efficiency between AC and DC buses; however, such efficiency value depends on the amount of power to be converted. Taking the experience from the large-scale PV system connected to the grid, the simplified mathematical formula presented in (8.29) has been used [32], where the value of the

parameters m_0 and m_1 has been calculated by using the experimental results reported in [33].

$$\eta_c = \frac{P_{l(t)}}{m_0 P_c^r + (1 + m_1) P_{l(t)}} \tag{8.29}$$

Results obtained from parameter identification process carried out to determine m_0 and m_1 are shown in Fig. 8.5: finding m_0 = 0.015784 and m_1 = 0.078815; the identification method was based on Generalized Reduced Gradient (GRG) algorithm [34].

"Insert Fig. 8.5 here"

8.3. Hybrid Energy Systems Sizing and Optimization

In this chapter, the proposed work is going to illustrate mono-objective optimization, which is carried out by taking into account NPC during the project's lifetime (j); satisfying a determined reliability level (EIU_{tr}), the definitions of all these concepts are presented in (8.30)-(8.32) [16].

$$NPC = \frac{(ACC + ARC + AMC)}{CRF_{(i,j)}} \tag{8.30}$$

$$CRF_{(i,j)} = \frac{i(1+i)^j}{(1+i)^j - 1} \tag{8.31}$$

$$EIU = \frac{\sum_t ENS_{(t)}}{\sum_t P_{l(t)}} \tag{8.32}$$

Optimization technique to be used is GA; it could be implemented by following the algorithm presented as follows [35]:

- Step 1: Create the initial population using integer random generation, so that $1 \leq G_1 \leq G_1^{max}$, $0 \leq G_2 \leq G_2^{max}$, $1 \leq G_3 \leq G_3^{max}$, $0 \leq G_4 \leq G_4^{max}$, $1 \leq G_5 \leq G_5^{max}$, and $1 \leq G_6 \leq G_6^{max}$; where a determined individual (q) is represented by the six chromosomes arranged as follows: $|G_1|G_2|G_3|G_4|G_5|G_6|$.
- Step 2: Analyze the first generation by setting $y \leftarrow 1$.

- Step 3: Estimate the behavior of each individual in the population by means of a simulation on a yearly basis in order to calculate NPC and Energy Index of Unreliability (EIU).
- Step 4: Calculate fitness using (8.33) for each individual, if ($EIU < EIU_{tr}$); then a high value of NPC is artificially assigned ($NPC \rightarrow \infty$).

$$F_{I(q)} = \frac{(Q+1) - q}{\sum_{S=1}^{Q}\{(Q+1) - s\}}; \;\; q = 1,2, \ldots, Q \tag{8.33}$$

- Step 5: Carry out reproduction, crossing, and mutation processes according to the corresponding rates.
- Step 6: If ($y < Y$); then $y \leftarrow y + 1$ and go to step 3; else stop.

8.4. Rural Electrification in a Remote Community

In Morocco a rural electrification project was carried out that allowed this country to increase its rural electrification rate from 18% in 1995 to 97.4% in 2011 [36]. In this section, the optimal sizing of HPS is illustrated by analyzing a hypothetical case study that consists of providing electric service to a small rural clinic located in Tangiers (Latitude: 35°, 46' N and Longitude: 5°, 48' W). The expected hourly electric consumption of the rural clinic is shown in Fig. 8.6. Hourly solar radiation data for the optimal slope of 60º (and azimuth 0º) was synthetically generated by using the method proposed by Graham and Hollands [37] combined with information provided by National Aeronautics and Space Administration (NASA) [38], which is shown in Fig. 8.7. Regarding ambient temperature: as in the case of solar radiation, average, maximum and minimum values, such data were obtained from NASA database (Fig. 8.8) and combined with the model proposed by Erbs *et al.* [39], which is presented in (8.34) and (8.35).

"Insert Fig. 8.6 here"

"Insert Fig. 8.7 here"

"Insert Fig. 8.8 here"

$$a = 2\pi(h-1)/24 \tag{8.34}$$

$$\begin{aligned} T_{a(t)} = T_a^{avg} + \left(T_a^{max} - T_a^{min}\right) \\ \times[0.4632\cos(a-3.805) + 0.0984\cos(2a-0.360) \\ + 0.0168\cos(3a-0.822) + 0.0139\cos(4a-3.513)] \end{aligned} \tag{8.35}$$

Wind speed time series was synthetically generated by using the model developed by Nfaoui *et al.* [40], which is based on the Autoregressive Model (AR) model of order *p* (AR(*p*)) shown in (8.36).

$$\overline{w}_{(t)} = \emptyset_1\overline{w}_{(t-1)} + \emptyset_2\overline{w}_{(t-2)} + \cdots + \emptyset_p\overline{w}_{(t-p)} + \varepsilon_{(t)} \tag{8.36}$$

Let $w_{(t)}$ be the wind speed time series measured in situ, a transformation and standardization processes are required to obtain the parameters of the corresponding AR(*p*) model. These processes could be briefly described in (8.37), where the transformation is carried by elevating $w_{(t)}$ at the power m, so that a Gaussian Probability Density Function (PDF) is obtained.

Then, the transformed time series is normalized by using the hourly mean (μ_h) and the hourly standard deviation (σ_h) as shown in (8.37); it is important to note that these signals are considered to be periodical, hence: $\mu_{(1)} = \mu_{(25)}$, $\mu_{(2)} = \mu_{(26)}$, and $\sigma_{(1)} = \sigma_{(25)}$, $\sigma_{(2)} = \sigma_{(26)}$, and so on.

$$\overline{w}_{(t)} = \frac{\left[w_{(t)}\right]^m - \mu_{(h)}}{\sigma_{(h)}}; t = 1, \ldots, T; h = 1,2, \ldots, H \tag{8.37}$$

However, the goal of this work is not to fit the AR(*p*) model from measured data; on the contrary, it needs to undo this process in order to obtain a simulation of Typical Meteorological Year (TMY) for Tangiers from data already reported in the literature. Wind speed is statistically described by Weibull PDF, shown in (8.38).

$$F_{W(w)} = 1 - exp\left(-\left[\frac{w}{\theta}\right]^{\lambda}\right). \quad (8.38)$$

Table 8.1 presents the information related to Weibull PDF and autocorrelation function for each month: specifically, the factors for the first two lags. According to the original work [40], the order of AR(p) model is two (p=2); then using r_1 and r_2 from Table 8.1, the parameters $\emptyset_1$ and $\emptyset_2$, and the standard deviation for the white noise ($\varepsilon_{(t)}$) can be estimated.

Once all parameters of (8.36) are known, a transformed and standardized time series could be synthetically generated. After that, the obtained series is multiplied by $\sigma_{(h)}$ and summed to $\mu_{(h)}$ (equation (8.37)). Hence, a transformed time series is obtained, or, in other words, a time series with Gaussian PDF. In order to obtain a Weibull PDF with the parameters presented in Table 8.1, each value of the transformed time series is evaluated on (8.39) [41]; this probabilistic transformation allows modifying the transformed time series from a Gaussian PDF to a Weibull PDF of (8.38). This procedure is repeated for each month of the year using the data of Table 8.1, and the hourly values of $\mu_{(h)}$ and $\sigma_{(h)}$ reported in Tables 8.2 and 8.3.

$$\widetilde{w}_{(t)} = F_W^{-1}\left[F_N\left(\mu_{(h)} + \sigma_{(h)}\overline{w}_{(t)}\right)\right]. \quad (8.39)$$

"Insert Table 8.1"

"Insert Table 8.2"

"Insert Table 8.3"

The most important results obtained from the aforementioned procedure for the simulation of wind speed time series are shown in Figs 8.9-8.11. Fig. 8.9 presents PDF of simulated wind speed time series with scale factor of 7.101 m/s and shape factor of 1.65. Fig. 8.10 shows the simple and partial autocorrelation functions, which effectively

correspond to a AR(2) model, and Fig. 8.11 presents the hourly average profile for each season of the year.

"Insert Fig. 8.9 here"

"Insert Fig. 8.10 here"

"Insert Fig. 8.11 here"

Simulation and optimization processes were carried out by considering the values presented in Table 8.4. In a general sense, a single battery string of 50 Ah and a single PV string of 50 Wp were defined so that, through the optimization process, the optimal capacity of the wind turbine (between 0 W and 1,000 W), the optimal number of battery strings (between 1 and 10), and the optimal number of PV strings (between 0 and 20) were determined.

The wind turbine was modeled by means of the normalized power curve of Fig. 8.3; hence, $P_w^r \epsilon$[0 W; 1,000 W]. Similarly, the PV generator was modeled by using (8.1)-(8.4) and scaled according to the number of PV strings ($N_{pvp} \epsilon$ [0; 20]), while the battery bank was modeled by using the parameters of OGi batteries presented in [23], whereas battery bank size is obtained by scaling the results for a single string according to the number of battery strings (N_{bp} ϵ [1; 20]).

Regarding the simulation process, taking into account the available resources and load demand at a determined time instant, the current to be absorbed or delivered by the battery bank is determined by using system voltage (V_{sys}); then the current to be absorbed or delivered by a single cell ($I_{sys(t)}$) is estimated by using the number of battery strings. After that, the current $I_{b(t)}$ is obtained from the evaluation of the control actions of the charge controller (bulk, absorption, equalization, and float charges). Finally, this current value is used to evaluate the impact of the different aging mechanisms on battery lifetime.

"Insert Table 8.4 here"

Technical and economic analysis were carried out by considering wind turbine capital cost as $4,200/kW and a lifetime of 10 years, replacement cost US$3,300/kW, and Operation and Maintenance (O&M) cost as US$120/kW. Capital and replacement costs of the power converter were estimated by assuming it as US$875/kW and a lifetime of 10 years, while O&M cost was assumed to be 1% of the initial investment.

Regarding BESS, capital and replacement costs were estimated as US$100/kWh and O&M was assumed to be 1% of the initial investment. Capital and replacement costs of PV panels were assumed as US$1.5/W, and O&M cost was assumed to be 1% of the initial investment with a lifetime of 20 years. Nominal interest rate considered was 7% with an inflation rate of 3%.

Convergence of GA during the optimization process is shown in Fig. 8.12, where the optimal design corresponds to a PV/BESS system with a PV generator with 7 strings of 50 Wp (total 350 Wp) and a battery bank with 9 strings of 50Ah (total 5.4 kWh) with an estimated NPC of US$3,924 (levelized cost of energy US$0.53/kWh).

The expected battery lifetime of the optimal solution is 3.42 years. Simulation and optimization models were implemented in MATLAB® in a standard personal computer provided with an i7-3630QM CPU at 2.40 GHz, 8 GB of RAM and 64-bit operating system, obtaining similar results to those provided by iHOGA software [11] in less than one minute.

"Insert Fig. 8.12 here"

The hourly PV output power is shown in Fig. 8.13 (all the years are considered similar). SOC time series during the first four years of the optimized solution is presented in Fig. 8.14, and Fig. 8.15 shows the SOC of 10 days of January of the 3rd year. As can be observed, the battery bank remains with a very high SOC during its operative lifetime

with a cycle operation during short-time intervals without deep discharges; as a consequence, discharging capacity is mainly influenced by the corrosion process (Fig. 8.16), while the number of bad charges (Fig. 8.17) impacts battery bank lifetime just at its end, which could be identified by analyzing the number of weighted cycles (Fig. 8.18).

In order to get a cost-effective solution, on one hand GA looks for those configurations that are able to extend the battery bank lifetime as long as possible, so that deep discharges and the operation during long-time under low SOC are avoided. On the other hand, as the battery lifetime is simulated all over its float lifetime on an hourly basis, it represents an important increment on the computational burden of the optimization problem.

"Insert Fig. 8.13 here"

"Insert Fig. 8.14 here"

"Insert Fig. 8.15 here"

"Insert Fig. 8.16 here"

"Insert Fig. 8.17 here"

"Insert Fig. 8.18 here"

8.5. Conclusions

Renewable energy systems are a good option to provide electric service in a sustainable way by taking advantage of the natural resources locally available. A direct application of this philosophy is rural electrification, in which electricity in remote areas is provided by means of autonomous systems, EDN extensions, or mini-grids installation. To carry out this task in a cost-effective manner, simulation and optimization techniques are applied by considering an estimation of the renewable resources, ambient temperature, and load demand, as well as the behavior of the different components of the system

such as wind turbine, PV generator, and BESS, so that a reliable and affordable energy system is finally installed.

All of these topics have been studied in this chapter through the analysis of an autonomous HPS composed of a wind turbine, a PV generator, a storage system based on lead-acid batteries, a power converter, and a dump load. Wind speed and solar radiation time series were synthetically generated by using information previously reported in the literature and public databases for the location under analysis (Tangiers, Morocco); variations on the efficiency of the power converter with the AC load, as well as charge controller operation including bulk, absorption, equalization, and float charges, battery bank performance and aging mechanisms, were integrated in a optimization model based on GA. From the obtained results, it was possible to observe how the optimization algorithm looks for those HPS configurations able to prolong battery bank lifetime by avoiding the operation of it at low SOC during long time periods.

List of symbols

Δt	Time step (1h)
t	Index for time of the year $t \in [1,T]$
T	Total simulation time (8760h)
h	Index for time of the day $h \in [1,H]$
H	Total daily time (24h)
q	Index for each individual in the population
Q	Total number of individuals in the population (Population size)
Y	Total number of generations of GA
y	Index for each generation of GA
$P_{d(t)}$	Power consumed by dump load at time t (W)
$P_{l(t)}$	Load demand at time t (W)
$ENS_{(t)}$	Energy not supplied at time t (Wh)
N_{pvp}	Number of PV strings
$P_{pv(t)}$	PV generation of a single panel at time t (W)
A_{pv}	Area of PV panel (m^2)
P_{STC}	Power generation of PV panel under standard test conditions (W)
$G_{(t)}$	Incident solar radiation at time t (kW/m^2)
α	Temperature coefficient of power (%/°C)
$T_{c(t)}$	PV cell temperature (°C)

$T_{a(t)}$	Ambient temperature (°C)
T_a^{avg}	Daily mean ambient temperature (°C)
T_a^{max}	Daily maximum ambient temperature (°C)
T_a^{min}	Daily minimum ambient temperature (°C)
T_{NOCT}	Nominal operating cell temperature (°C)
$WT_{(w)}$	Wind turbine power curve (W)
P_w^r	Rated power of wind turbine (W)
$P_{w(t)}$	Wind power production at time t (W)
$w_{(t)}$	Wind speed at time t (m/s)
$\overline{w}_{(t)}$	Transformed and standardized wind speed at time t (m/s)
$\widetilde{w}_{(t)}$	Simulated wind speed at time t (m/s)
m	Transformation power of wind speed time series
$\emptyset_1, \dots, \emptyset_p$	Autoregressive coefficients of AR(p) model
$\varepsilon_{(t)}$	White noise autoregressive model at time t
μ_h	Hourly average of transformed wind speed at time h (m/s)
σ_h	Hourly standard deviation of wind speed at time h (m/s)
F_W	Cumulative Weibull distribution function
F_W^{-1}	Inverse Weibull distribution function
F_N	Cumulative normal distribution function
λ	Shape factor of Weilbull distribution
θ	Scale factor of Weilbull distribution (m/s)
r_1	Value of autocorrelation function in one lag
r_2	Value of autocorrelation function in two lags
η_c	Efficiency of power inverter
P_c^r	Rated power of inverter (W)
m_0, m_1	Parameters of converter model
$P_{b(t)}$	Power from/to battery bank at time t (W)
$V_{b(t)}$	Battery voltage at time t (V)
V_0	Open-circuit voltage (V)
V_0^c	Corrosion open-circuit voltage (V)
$\bar{V}_b^G$	Nominal gassing voltage (V)
V_b^r	Reference voltage for reduction of acid stratification (V)
V_{sys}	Nominal voltage of the system (V)
$\Delta W_{(t)}$	Effective layer thickness
ΔW_{lim}	Effective layer thickness at the end of battery float life
k_s	Corrosion speed parameter
$k(\cdot)$	Lander corrosion speed vs. voltage curve
k_s^{lim}	Corrosion speed parameter at float voltage
g	Electrolyte proportionality constant (V)
$DOD_{(t)}$	Depth of discharge of the battery at time t
$SOC_{(t)}$	State of charge of the battery at time t
SOC_{min}	Minimum SOC of battery bank
SOC_{max}	Maximum SOC reached during fully-charged period
$I_{b(t)}$	Current from/to battery bank at time t (A)
$I_{b(t)}^G$	Gassing current at time t (A)
$\bar{I}_{b(0)}^G$	Normalized gassing current respect to a 100 Ah battery (A)
$I_{b(t)}^d$	Discharging current at time t (A)

I_b^r	Reference current of the battery (A)
$I_{sys(t)}$	Current supplied or demanded for a single battery at time t
$\rho_{c(t)}, \rho_{d(t)}$	Aggregated internal resistance for charging and discharging (Ω Ah)
ρ_{lim}	Internal resistance at the end of battery float life (Ω Ah)
$\Delta\rho_{(t)}$	Increment in the internal resistance due to corrosion (Ω Ah)
M_c, M_d	Charge-transfer overvoltage coefficient for charging and discharging
$C_c, C_{d(t)}$	Normalized capacity for charging and discharging, respectively
C_N	Nominal capacity of the battery (Ah) (Capacity in 10h)
$\bar{T}_N^G$	Nominal gassing temperature (K)
$\bar{T}_N^C$	Nominal corrosion temperature (K)
c_{pls}	Parameter for the increment of acid stratification
$k_{s,T}$	Temperature factor (1/K)
c_u	Voltage coefficient (1/V)
c_T	Temperature coefficient (1/K)
c_Z	Parameter used in the estimation of capacity loss due to degradation
c_{min}	Parameter for the reduction of acid stratification by gassing
c_{SOCmin}	Coefficient to represent influence of the minimum state of charge in state of charge weighting factor (1/h)
c_{SOCo}	Increase in $f_{(t)}^{SOC}$ factor at state of charge equal to zero (1/h)
C_{lim}^c	Lost capacity at the end of battery float life due to corrosion
C_{lim}^d	Loss of capacity at the end of battery float life due to degradation
$\Delta C_{(t)}^c$	Increment in the loss of capacity at time t due to corrosion
$\Delta C_{(t)}^d$	Increment in the loss of capacity at time t due to degradation
t_0	During a charging cycle, this is the time of the last full charge (h)
z_{IEC}	Number of lifetime cycles under standard conditions
$Z_{W(t)}$	Weighted number of cycles at time t
$f_{(t)}^{SOC}$	State of charge weighting factor
$f_{(t)}^{ACD}$	Factor for total impact of acid stratification
$f_{(t)}^{STR}$	Weighting factor for degree of acid stratification factor
$f_{(t)}^{PLS}$	Weighting factor for the increment of acid stratification
$f_{(t)}^{MIN}$	Weighting factor for the total decrement of acid stratification
$f_{(t)}^{MIN,G}$	Factor for the decrement of acid stratification at time t by gassing
$f_{(t)}^{MIN,D}$	Factor for the decrement of acid stratification at time t by diffusion
L_{flt}	Battery float life (yr)
n	Cumulative number of bad recharge cycles
D	Effective diffusion constant (m^2/s)
z	Height of the battery (cm)
a,s,x	Intermediate variables
N_{bp}	Number of battery strings
EIU	Energy index of unreliability
EIU_{tr}	Required EIU of the hybrid system
V_{abs}	Voltage during absorption stage of charge controller (V)
V_{eql}	Voltage during equalization stage of charge controller (V)
V_{flt}	Voltage during float stage of charge controller (V)
t_{abs}	Duration time of absorption stage (h)
t_{eql}	Duration time of equalization stage (h)

i	Real interest rate
j	Project lifetime (yr)
$CRF_{(i,j)}$	Capital recovery factor for real interest rate i and project lifetime j
NPC	Net present cost (US$)
ACC	Annualized capital cost (US$/yr)
ARC	Annualized replacement cost (US$/yr)
AMC	Annualized maintenance cost (US$/yr)
ΔK	Crossing rate of genetic algorithm
ΔM	Mutation rate of genetic algorithm
$F_{I(q)}$	Fitness of individual q
G_1	Chromosome to represent the type of wind turbine
G_2	Chromosome to represent number of wind turbine
G_3	Chromosome to represent the type of photovoltaic panel
G_4	Chromosome to represent the number of photovoltaic panel strings
G_5	Chromosome to represent the type of batteries
G_6	Chromosome to represent the number of battery strings
G_1^{max}	Maximum amount of wind turbine types
G_2^{max}	Maximum amount of wind turbines
G_3^{max}	Maximum amount of photovoltaic panel types
G_4^{max}	Maximum amount of photovoltaic panel strings
G_5^{max}	Maximum amount of battery types
G_6^{max}	Maximum amount of battery strings

Acknowledgment

This work was supported by FEDER funds through COMPETE and by Portuguese funds through FCT, under FCOMP-01-0124-FEDER-020282 (PTDC/EEA-EEL/118519/2010), PEst-OE/EEI/LA0021/2013 and SFRH/BPD/103079/2014. Moreover, the research leading to these results has received funding from the EU Seventh Framework Programme FP7/2007-2013 under grant agreement no. 309048. This work was also supported by the Ministerio de Economía y Competitividad of the Spanish Government under Project ENE2013-48517-C2-1-R.

References

[1] International Energy Agency, World Energy Outlook 2015, Paris, France, 2015.

[2] The World Bank, The welfare impact of rural electrification: A reassessment of the costs and benefits, Washington DC, United States, 2008.

[3] The World Bank, Implementation completion and results report on a credit in the amount of SDR 27.9 million and a global environment facility grant in the amount of

US$ 5.75 million to the Kingdom of Cambodia for a rural electrification and transmission project, Washington DC, United States, 2012.

[4] The World Bank, Project performance assessment report, The Peoples' Republic of Bangladesh. Rural electrification and renewable energy development project. Power sector development technical assistance project. Power sector development policy credit, Washington DC, United States, 2014.

[5] The World Bank, Implementation completion and results report on an IDA grant in the amount of SDR 7.0 million and a global environment facility grant in the amount of US$ 3.75 million and an AUSAID grant co-financing in the amount of US$ 9.42 million to the Lao People's Democratic Republic for a rural electrification phase I project of the rural electrification (APL) program, Washington DC, United States, 2013.

[6] The World Bank, Rural electrification phase II project of the rural electrification (APL) program. Lao People's Democratic Republic, Washington DC, United States, 2015.

[7] The World Bank, Implementation completion and results report on a loan in the amount of US$ 50 million and a global environmental facility grant in the amount of US$10 million to the Republic of Peru for a rural electrification project, Washington DC, United States, 2015.

[8] The World Bank, Project paper for a small RETF grant in the amount of US$ 4.7 million equivalent to the Republic of Vanuatu for a rural electrification project, Washington DC, United States, 2014.

[9] Homer Energy, The Homer Pro® microgrid software. < www.homerenergy.com/>, 2016 (accessed 09.20.2016).

[10] J.F. Manwell, A. Rogers, G. Hayman, C.T. Avelar, J.G. McGowan, Hybrid2: A hybrid system simulation model: Theory manual, Renewable Energy Research Laboratory University of Massachusetts and National Renewable Energy Laboratory, Massachusetts, 1998.

[11] Department of Electrical Engineering University of Zaragoza, Software iHOGA. <http://personal.unizar.es/rdufo/index.php?lang=en>, 2016 (accessed 09.20.2016).

[12] University of Oldenburg, What is INSEL? <http://insel.eu/index.php?id=301&L=1>, 2016 (accessed 09.20.2016).

[13] Thermal Energy System Specialists, LLC, What is TRNSYS? <http://www.trnsys.com/>, 2016 (accessed 09.20.2016).

[14] J.L. Bernal-Agustín, R. Dufo-López, Simulation and optimization of stand-alone hybrid renewable energy systems, Renew. Sust. Energ. Rev. 13 (2009) 2111-2118.

[15] A.C. Jimenez, K. Olson, Renewable energy for rural health clinics, National Renewable Energy Laboratory, Colorado, United States, 1998.

[16] T. Lambert, P. Gilman, P. Lilienthal, Micropower system modeling with HOMER, in: F.A. Farret, M.G. Simões (Eds.), Integration of alternative sources of energy, John Wiley & Sons Inc., NJ, United States, 2006, pp. 379-418.

[17] E. Lorenzo, Solar electricity: engineering of photovoltaic systems, Earthscan Publications Ltd, Seville, Spain, 1994.

[18] C.M. Shepherd, Design of primary and secondary cells II. An equation describing battery discharge, J. Electrochem. Soc. 112 (1965) 657-664.

[19] J.F. Manwell, J.G. McGowan, Lead acid battery storage model for hybrid energy systems, Sol. Energy. 50 (5) (1993) 399-405.

[20] J.B. Copetti, E. Lorenzo, F. Chenlo, A general battery model for PV system simulation, Prog. Photovoltaics Res. Appl. 1 (1993) 283-292.

[21] D. Guash, S. Silvestre, Dynamic battery model for photovoltaic applications, Prog. Photovoltaics Res. Appl. 11 (2003) 193-206.

[22] V. Svoboda, H. Wenzl, R. Kaiser, A. Jossen, I. Baring-Gould, J. Manwell, P. Lundsager, H. Bindner, T. Cronin, P. Nørgård, A. Ruddell, A. Perujo, K. Douglas, C. Rodrigues, A. Joyce, S. Tselepis, N. Van der Borg, F. Nieuwenhout, N. Wilmot, F. Mattera, D.U. Sauer, Operating conditions of batteries in off-grid renewable energy systems, Sol. Energy 81 (2007) 1409-1425.

[23] J. Schiffer, D.U. Sauer, H. Bindner, T. Cronin, P. Lundsager, R. Kaiser, Model prediction for ranking lead-acid batteries according to expected lifetime in renewable energy systems and autonomous power-supply systems, J. Power Sources 168 (2007) 66-78.

[24] R. Dufo-López, J.M. Lujano-Rojas, J.L. Bernal-Agustín, Comparison of different lead-acid battery lifetime prediction models for use in simulation of stand-alone photovoltaic systems, Appl. Energ. 115 (2014) 242-253.

[25] D.U. Sauer, H. Wenzl, Comparison of different approaches for lifetime prediction of electrochemical systems-Using lead-acid batteries as example, J. Power Sources 176 (2008) 534-546.

[26] H. Bindner, T. Cronin, P. Lundsager, J.F. Manwell, U. Abdulwahid, I. Baring-Gould, Lifetime modelling of lead acid batteries. Denmark National Laboratory Risø, Roskilde, Denmark, 2005.

[27] A. Andersson. Battery lifetime modelling. Denmark National Laboratory Risø, Roskilde, Denmark, 2006.

[28] J.J. Lander, Further studies on the anodic corrosion of lead in H2SO4 solutions, J. Electrochem. Soc. 103 (1) (1956) 1-8.

[29] Deltran Corporation, Battery charging basic and charging algorithm fundamentals, DeLand FL, United States, 2002.

[30] H. Masheleni, X.F. Carelse, Microcontroller-based charge controller for stand-alone photovoltaic systems, Sol. Energy 61 (4) (1997) 225-230.

[31] B.J. Huang, P.C. Hsu, M.S. Wu, P.Y. Ho, System dynamic model and charging control of lead-acid battery for stand-alone solar PV system, Sol. Energy 84 (2010) 822-830.

[32] J.M. Lujano-Rojas, C. Monteiro, R. Dufo-López, J.L. Bernal-Agustín, Optimum load management strategy for wind/diesel/battery hybrid power systems, Renew. Energ. 44 (2012) 288-295.

[33] G.A. Rampinelli, A. Krenzinger, F. Chenlo-Romero, Mathematical models for efficiency of inverters used in grid connected photovoltaic systems, Renew. Sust. Energ. Rev. 34 (2014) 578-587.

[34] J.S. Arora, Introduction to optimum design, Academic Press, Massachusetts, United States, 2012.

[35] R. Dufo-López, J.L. Bernal-Agustín, Design and control strategies of PV-Diesel systems using genetic algorithms, Sol. Energy 79 (2005) 33-46.

[36] C.-C. Cîrlig, Solar energy development in Morocco, Library of the European Parliament. European Union, 2013.

[37] V.A. Graham, K.G.T. Hollands, A method to generate synthetic hourly solar radiation globally, Sol. Energy 44 (6) (1990) 333-341.

[38] National Aeronautics and Space Administration (NASA), NASA Surface meteorology and solar Energy.
<https://eosweb.larc.nasa.gov/cgi-bin/sse/grid.cgi?email=na>,
2016 (accessed 09.20.2016).

[39] D.G. Erbs, S.A. Klein, W.A. Beckman, Estimation of degree day and ambient temperature bin data from monthly-average temperatures, ASHRAE Journal 25 (1983) 60-65.

[40] H. Nfaoui, J. Buret, A.A.M. Sayigh, Stochastic simulation of hourly average wind speed sequences in Tangiers (Morocco), Sol. Energy 56 (3) (1996) 301-314.

[41] M. Rosenblatt M, Remarks on a multivariate transformation, Ann. Math. Statist. 23 (3) (1952) 470-472.

Tables

Table 8.1. Monthly Weibull and autocorrelation parameters [40].

Month	Shape factor (λ)	Scale factor (θ)	r_1	r_2
Jan	1.59	6.55	0.9	0.841
Feb	1.63	7.06	0.913	0.856
Mar	1.59	6.65	0.906	0.852
Apr	1.63	6.96	0.892	0.83
May	1.63	7.09	0.892	0.824
Jun	1.5	6.9	0.9	0.837
Jul	1.62	7.95	0.915	0.859
Aug	1.62	7.54	0.884	0.811
Sep	1.76	7.6	0.912	0.858
Oct	1.67	7.28	0.898	0.832
Nov	1.85	7.01	0.897	0.833
Dec	1.66	6.65	0.903	0.846

Table 8.2. Hourly average of transformed wind speed time series (μ_h) [40].

h	Jan	Feb	Mar	Apr	May	Jun	Jul	Aug	Sep	Oct	Nov	Dec
1	2.480	2.793	2.574	2.757	2.353	1.865	2.157	1.94	2.599	2.639	3.784	2.675
2	2.490	2.713	2.607	2.695	2.362	1.854	2.176	1.895	2.635	2.65	3.661	2.725
3	2.458	2.787	2.630	2.654	2.367	1.852	2.135	1.902	2.612	2.639	3.701	2.701
4	2.532	2.688	2.599	2.655	2.39	1.884	2.114	1.857	2.595	2.591	3.616	2.624
5	2.518	2.649	2.576	2.658	2.345	1.861	2.098	1.85	2.528	2.646	3.631	2.593
6	2.507	2.629	2.511	2.641	2.312	1.813	2.101	1.848	2.584	2.652	3.633	2.602
7	2.473	2.646	2.469	2.675	2.375	1.853	2.111	1.855	2.554	2.574	3.618	2.56
8	2.476	2.686	2.466	2.700	2.545	2.169	2.335	1.998	2.683	2.627	3.611	2.63
9	2.520	2.700	2.545	2.965	2.876	2.511	2.628	2.324	3.036	2.771	3.605	2.706
10	2.544	2.843	2.821	3.258	3.025	2.736	2.879	2.644	3.47	3.136	3.828	2.786
11	2.744	3.013	3.040	3.362	3.186	2.874	3.007	2.837	3.645	3.286	4.244	2.981
12	2.912	3.141	3.268	3.492	3.339	2.941	3.072	2.941	3.722	3.393	4.364	3.19
13	3.071	3.259	3.334	3.615	3.395	2.985	3.151	3.062	3.77	3.469	4.431	3.303
14	3.147	3.330	3.413	3.685	3.484	3.051	3.247	3.123	3.9	3.504	4.523	3.301
15	3.180	3.328	3.416	3.724	3.53	3.07	3.335	3.2	3.997	3.528	4.507	3.314
16	3.156	3.423	3.434	3.732	3.588	3.083	3.356	3.254	4.012	3.515	4.586	3.28
17	3.054	3.382	3.395	3.696	3.556	3.073	3.309	3.191	3.965	3.456	4.441	3.124
18	2.951	3.238	3.315	3.567	3.454	3.013	3.238	3.098	3.804	3.261	4.064	2.973
19	2.750	3.035	3.154	3.355	3.264	2.836	3.049	2.848	3.438	2.928	3.851	2.81
20	2.602	2.885	2.927	3.141	3.015	2.601	2.78	2.531	3.178	2.713	3.782	2.719
21	2.584	2.799	2.733	3.085	2.771	2.315	2.528	2.242	2.953	2.644	3.746	2.657
22	2.467	2.693	2.555	2.898	2.622	2.11	2.349	2.071	2.842	2.544	3.637	2.579
23	2.527	2.637	2.551	2.819	2.497	2.006	2.298	1.96	2.781	2.615	3.764	2.56
24	2.476	2.687	2.514	2.783	2.415	1.949	2.225	1.953	2.632	2.545	3.805	2.581

Table 8.3. Hourly standard deviation of transformed wind speed time series ($\sigma_{(h)}$) [40].

h	**Jan**	**Feb**	**Mar**	**Apr**	**May**	**Jun**	**Jul**	**Aug**	**Sep**	**Oct**	**Nov**	**Dec**
1	1.514	1.652	1.784	1.691	1.641	1.47	1.586	1.561	1.974	1.649	2.098	1.702
2	1.483	1.697	1.724	1.744	1.601	1.42	1.567	1.547	1.957	1.626	2.112	1.686
3	1.520	1.686	1.735	1.767	1.626	1.39	1.545	1.506	1.914	1.611	2.034	1.651
4	1.462	1.684	1.715	1.734	1.577	1.37	1.524	1.522	1.892	1.643	2.066	1.671
5	1.445	1.721	1.715	1.726	1.57	1.34	1.504	1.506	1.918	1.559	2.088	1.703
6	1.442	1.683	1.704	1.750	1.565	1.36	1.534	1.511	1.884	1.539	2.118	1.719
7	1.430	1.718	1.681	1.704	1.524	1.39	1.527	1.515	1.899	1.548	2.109	1.659
8	1.396	1.656	1.698	1.729	1.519	1.35	1.548	1.521	1.898	1.588	2.106	1.609
9	1.324	1.657	1.719	1.669	1.458	1.17	1.467	1.497	1.936	1.64	2.236	1.545
10	1.443	1.689	1.762	1.597	1.354	1.05	1.287	1.37	1.691	1.581	2.274	1.65
11	1.472	1.734	1.665	1.568	1.278	1.0345	1.235	1.234	1.64	1.447	2.2	1.696
12	1.490	1.653	1.590	1.475	1.227	1.019	1.229	1.198	1.567	1.379	2.18	1.626
13	1.397	1.555	1.518	1.416	1.136	1.026	1.208	1.174	1.54	1.229	2.09	1.56
14	1.325	1.527	1.501	1.411	1.166	1.012	1.176	1.154	1.541	1.324	2.096	1.596
15	1.305	1.483	1.531	1.438	1.166	1.001	1.18	1.138	1.536	1.389	2.098	1.573
16	1.326	1.471	1.560	1.397	1.146	1.014	1.176	1.112	1.556	1.41	2.081	1.542
17	1.369	1.493	1.604	1.384	1.176	1.031	1.182	1.129	1.529	1.398	2.103	1.597
18	1.386	1.540	1.649	1.394	1.217	1.101	1.212	1.155	1.578	1.431	2.197	1.571
19	1.356	1.528	1.592	1.431	1.276	1.072	1.253	1.262	1.691	1.528	2.215	1.625
20	1.471	1.643	1.653	1.505	1.362	1.204	1.404	1.365	1.804	1.608	2.196	1.64
21	1.495	1.675	1.721	1.571	1.515	1.32	1.519	1.482	1.931	1.646	2.292	1.654
22	1.544	1.732	1.772	1.663	1.528	1.379	1.568	1.557	2.004	1.647	2.231	1.703
23	1.493	1.792	1.780	1.762	1.609	1.406	1.623	1.581	1.997	1.643	2.135	1.708
24	1.495	1.722	1.762	1.410	1.625	1.443	1.626	1.577	2.02	1.66	2.145	1.697

Table 8.4. Simulation and optimization parameters.

Parameter	Value	Parameter	Value
V_0	2.1V	G_1^{max}	1
V_0^c	1.75V	G_2^{max}	21
$\bar{V}_b^G$	2.23V	G_3^{max}	1
V_b^r	2.5V	G_4^{max}	21
V_{sys}	12V	G_5^{max}	1
V_{abs}	2.4V	G_6^{max}	20
V_{eql}	2.45V	D	20×10^{-9} m^2s^{-1}
V_{flt}	2.25V	z	20 cm
P_c^r	100W	EIU_{tr}	1%
α	-0.43 %/°C	c_u	11 V^{-1}
T_{NOCT}	47 °C	c_T	0.06 K^{-1}
$\bar{T}_N^G$	298K	c_Z	5
$\bar{T}_N^C$	298K	c_{min}	0.1
$\bar{I}_{b(0)}^G$	20 mA	c_{SOCmin}	3.307×10^{-3} h^{-1}
I_b^r	10A ($I_{10} = C_{10}/10$)	c_{SOCo}	6.614×10^{-5} h^{-1}
t_{abs}	2h	c_{pls}	1/30
t_{eql}	2h	$k_{s,T}$	$ln(2)/15$ K^{-1}
g	0.076V	$\rho_{c(0)}$	0.42 ΩAh
i	3.8%	$\rho_{d(0)}$	0.699 ΩAh
j	20 yr	M_c	0.888
ΔK	90%	M_d	0.0464
ΔM	1%	C_c	1.001
Q	15	$C_{d(0)}$	1.75
Y	15	L_{flt}	10 yr (at 20ºC)
SOC_{min}	0.3	z_{IEC}	600

Figure

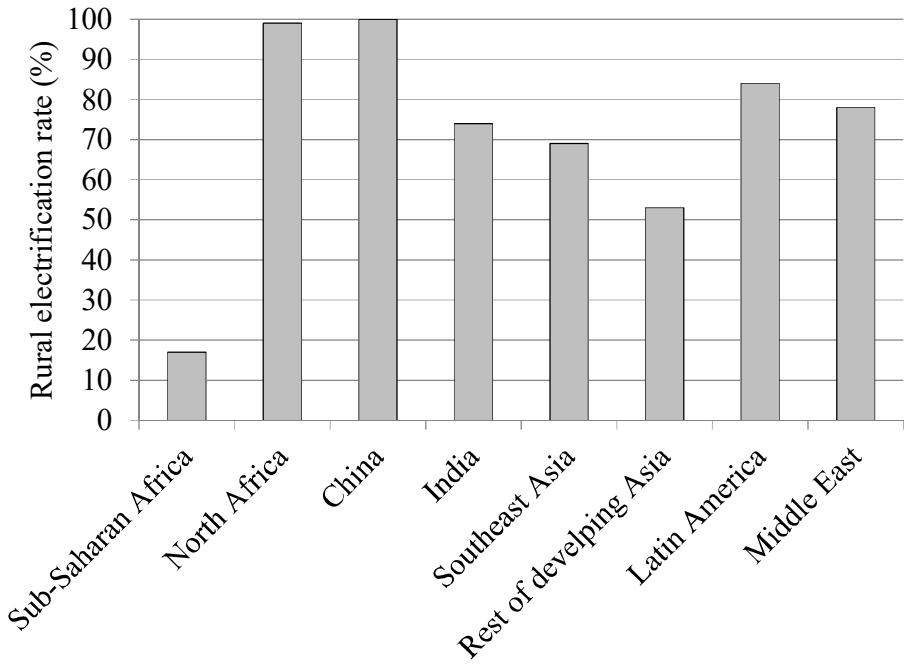

Fig. 8.1. Rural electrification rates per region [1].

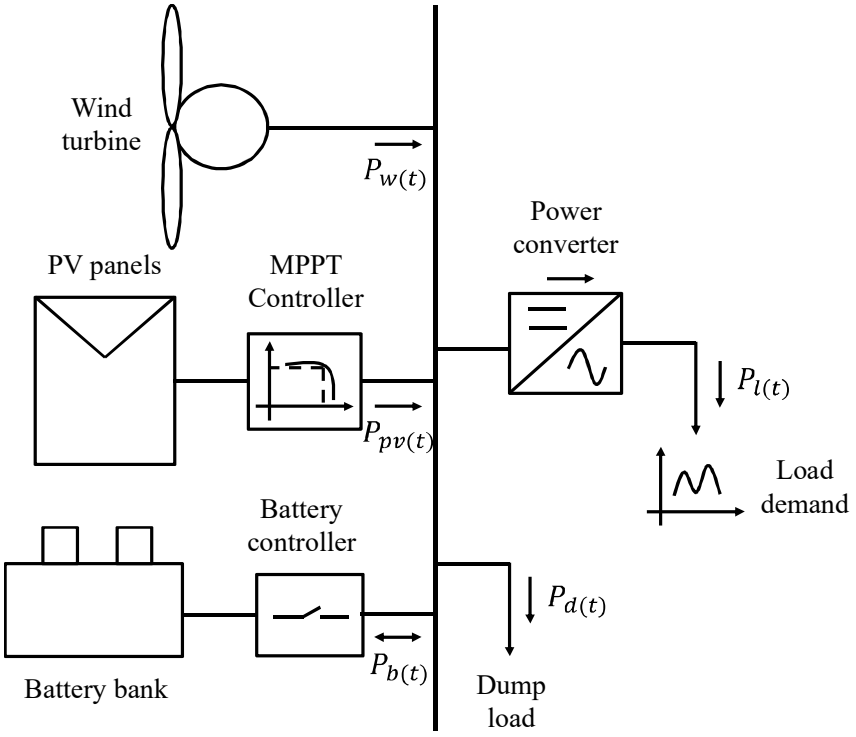

Fig. 8.2. Scheme of a typical HPS.

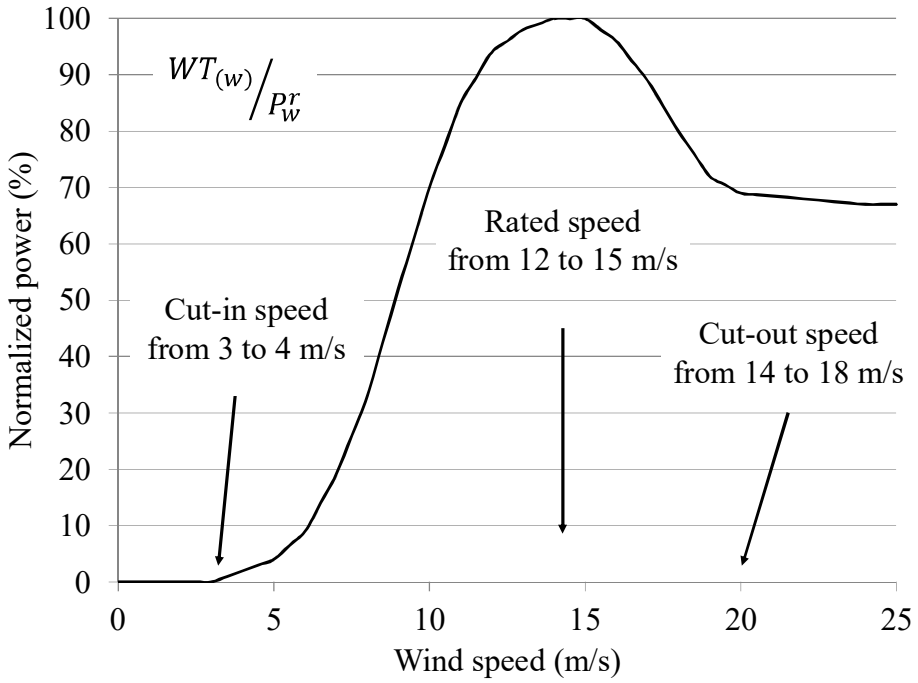

Fig. 8.3. Typical power curve of a small-capacity wind turbine.

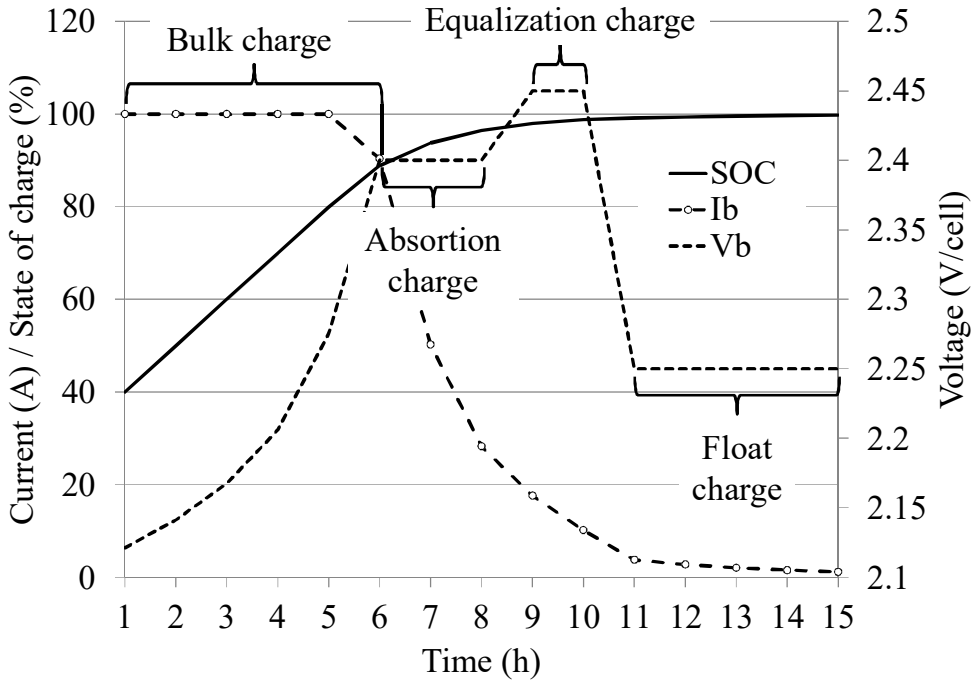

Fig. 8.4. Voltage, current, and SOC during charge of a single cell.

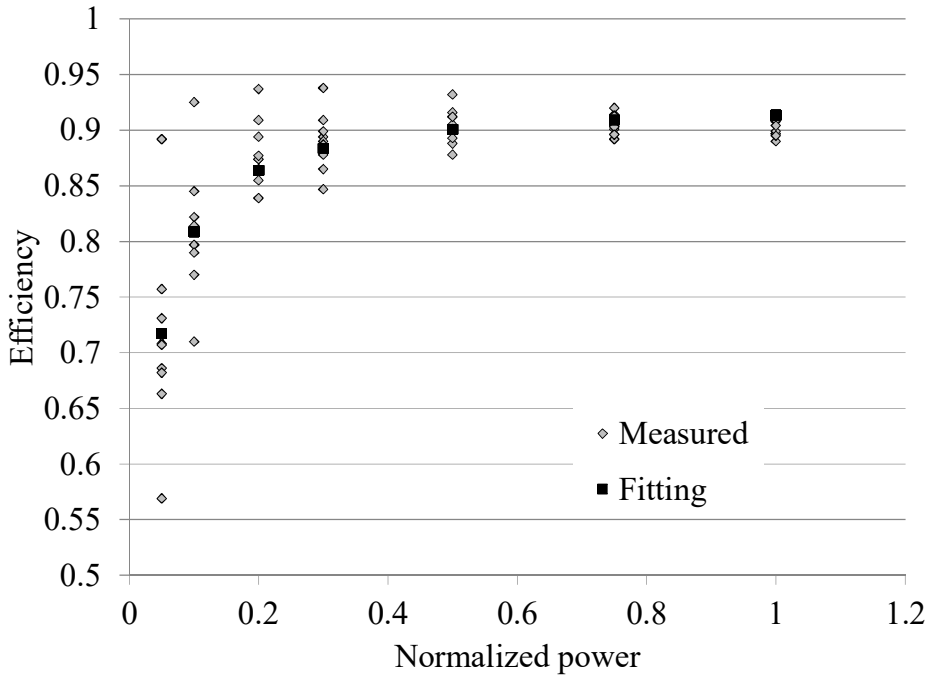

Fig. 8.5. Fitting of power inverter model.

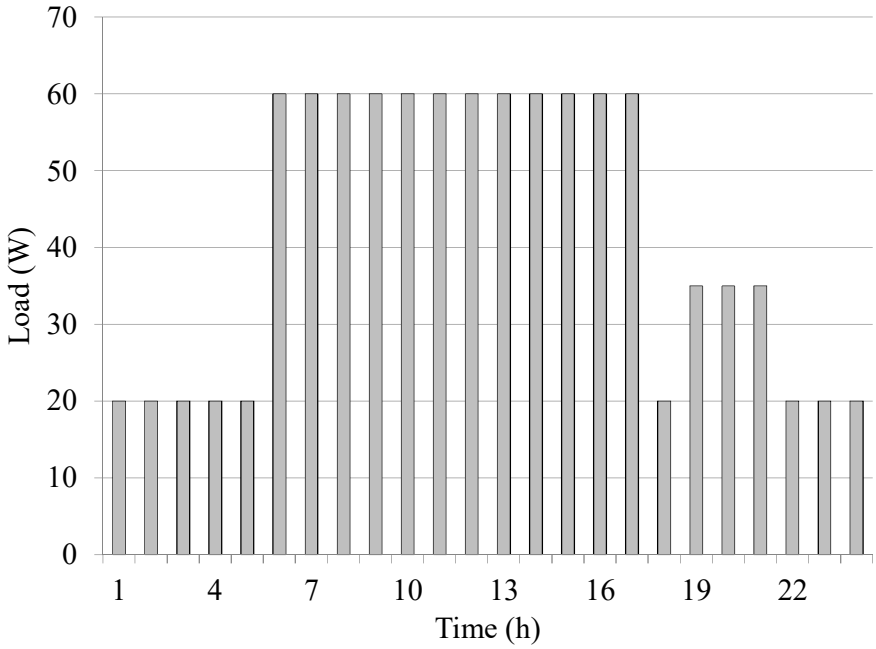

Fig. 8.6. Hourly load profile.

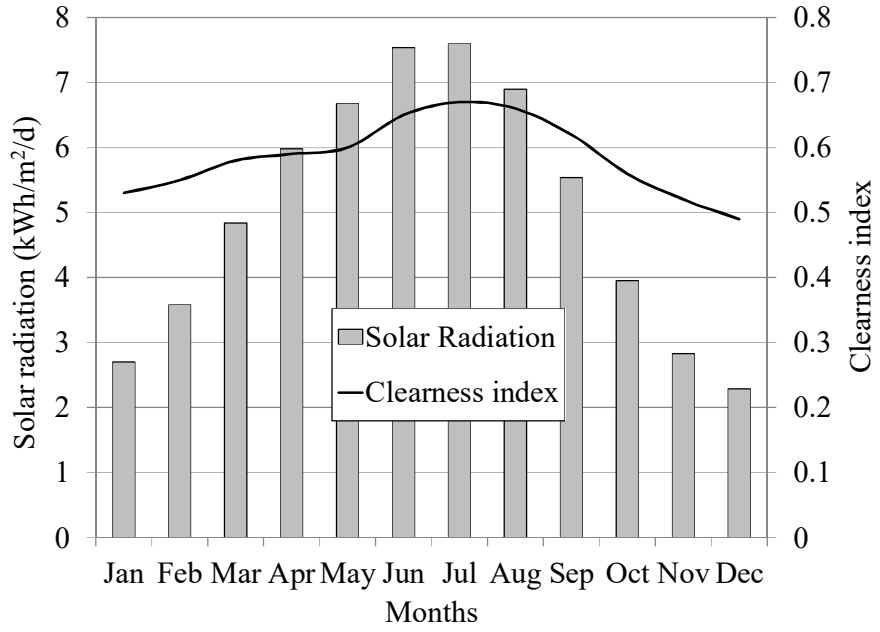

Fig. 8.7. Monthly solar radiation and clearness index.

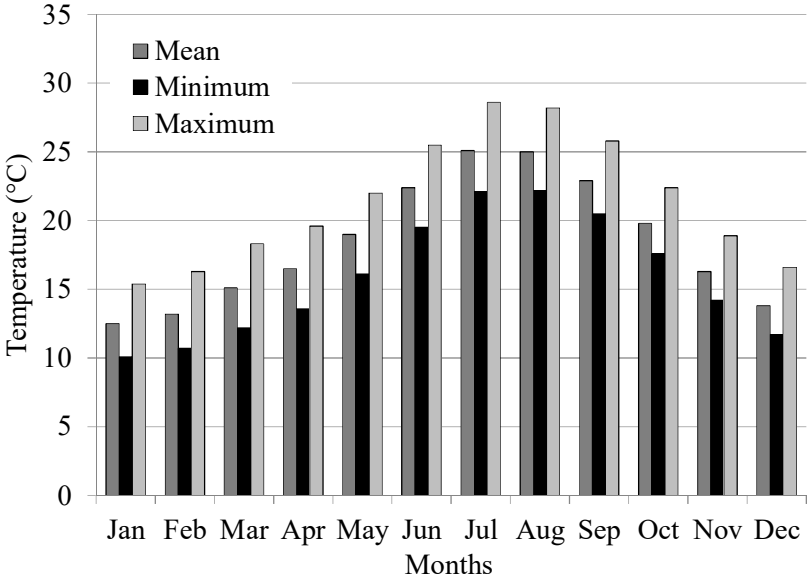

Fig. 8.8. Monthly average, maximum and minimum temperature.

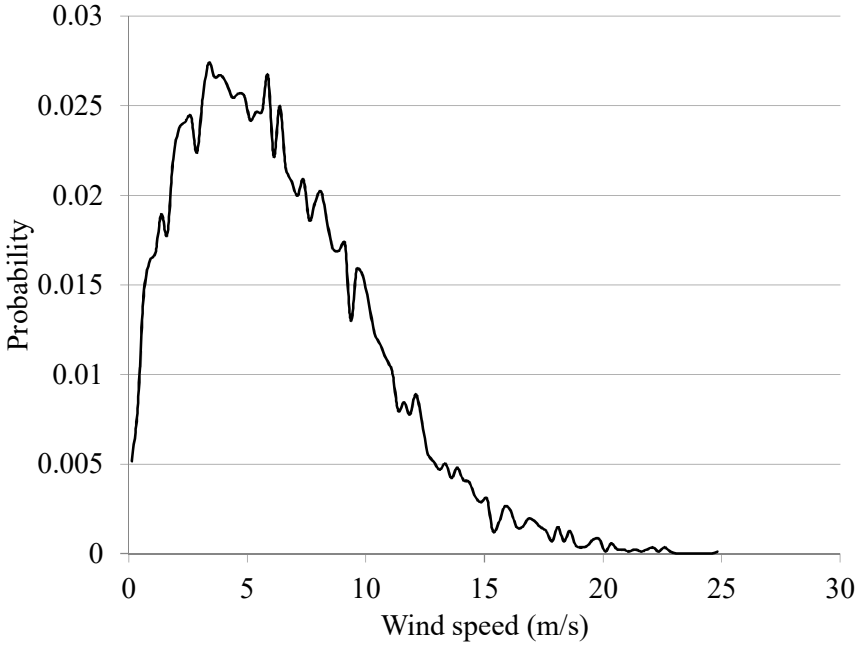

Fig. 8.9. Probability distribution of wind speed.

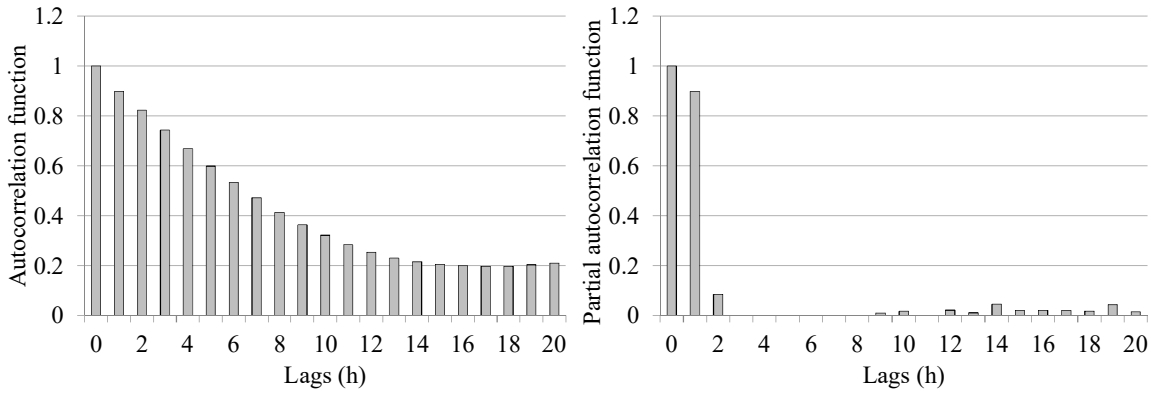

Fig. 8.10. Simple and partial autocorrelation functions of wind speed.

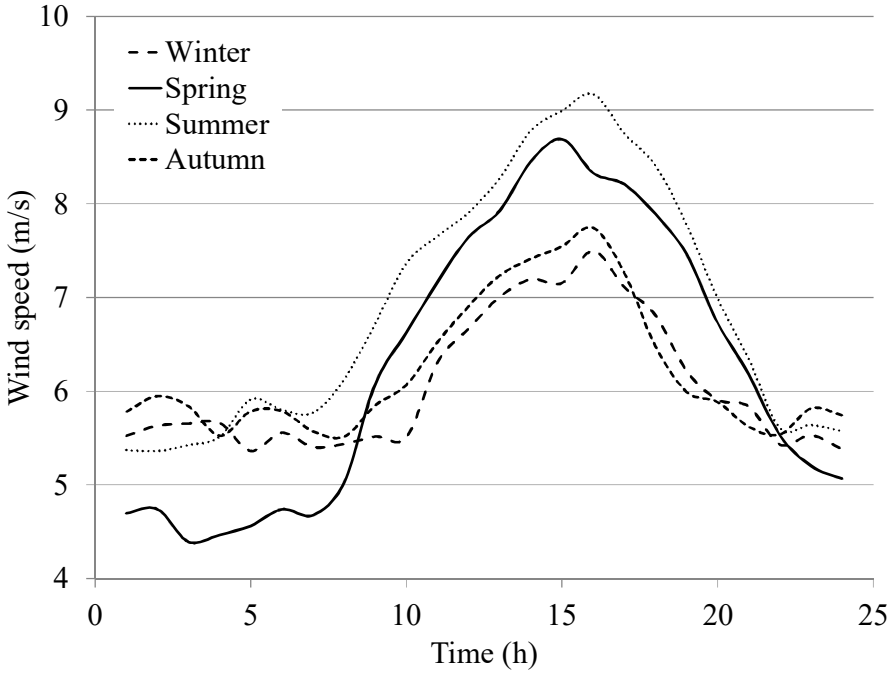

Fig. 8.11. Hourly profile of wind speed per season.

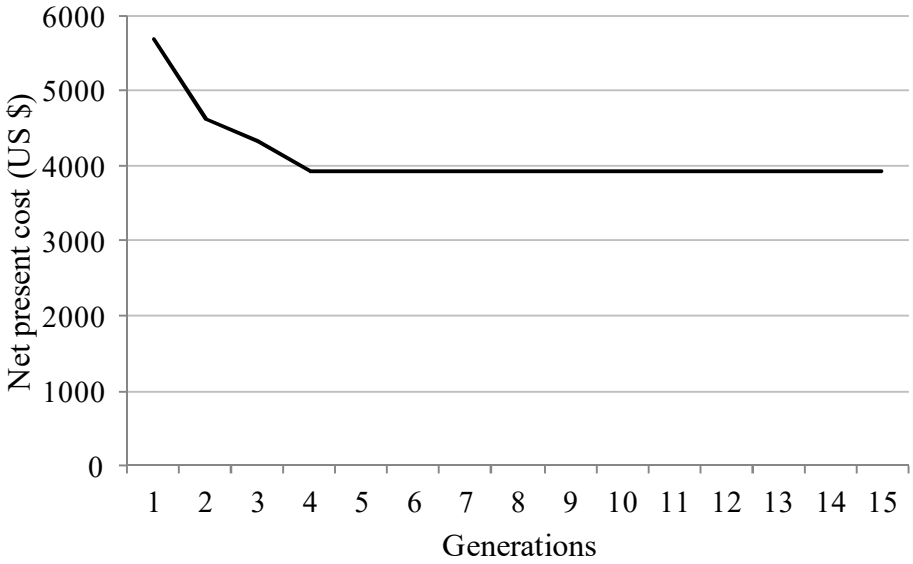

Fig. 8.12. Evolution of the implemented GA.

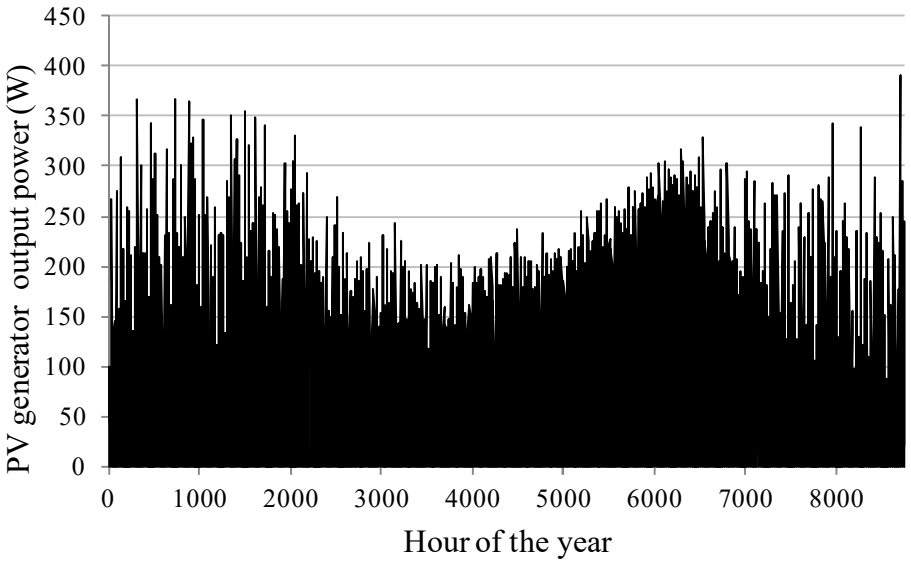

Fig. 8.13. PV generator output power during one year.

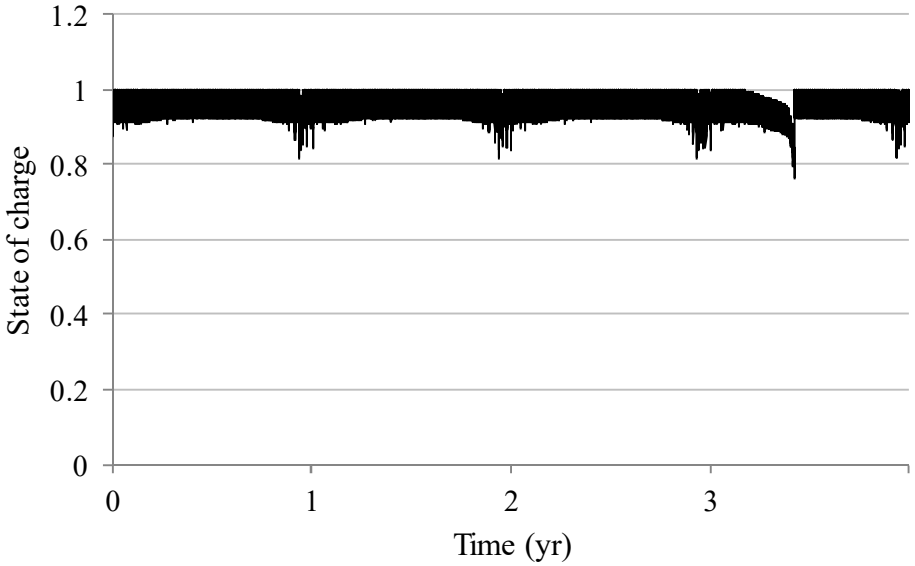

Fig. 8.14. State of charge of battery bank during the first 4 years.

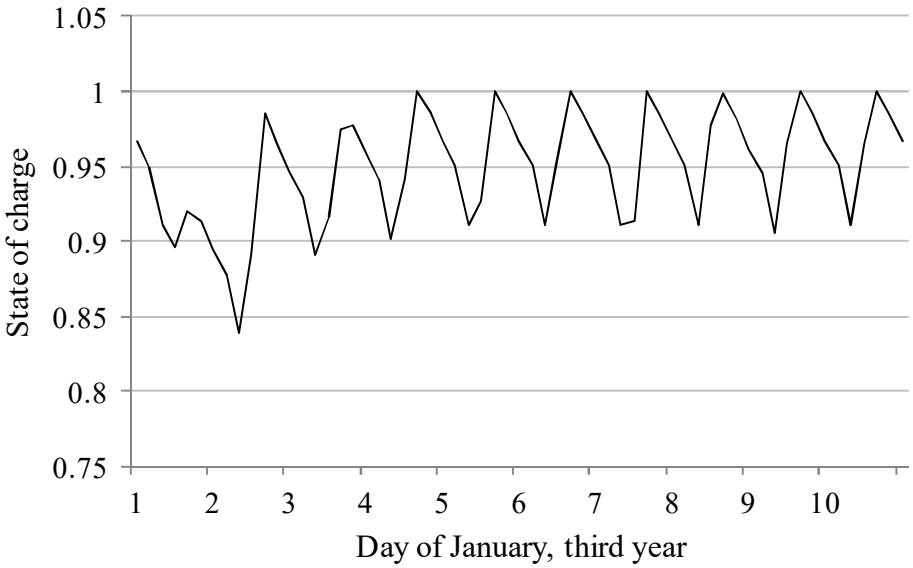

Fig. 8.15. State of charge of battery bank during 10 days of January of the 3rd year.

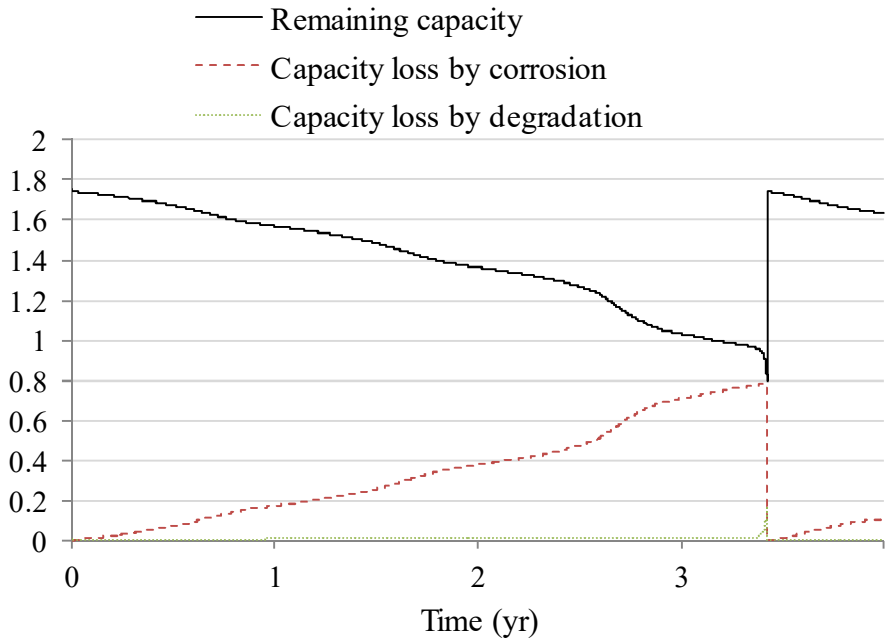

Fig. 8.16. Normalized capacity of battery bank.

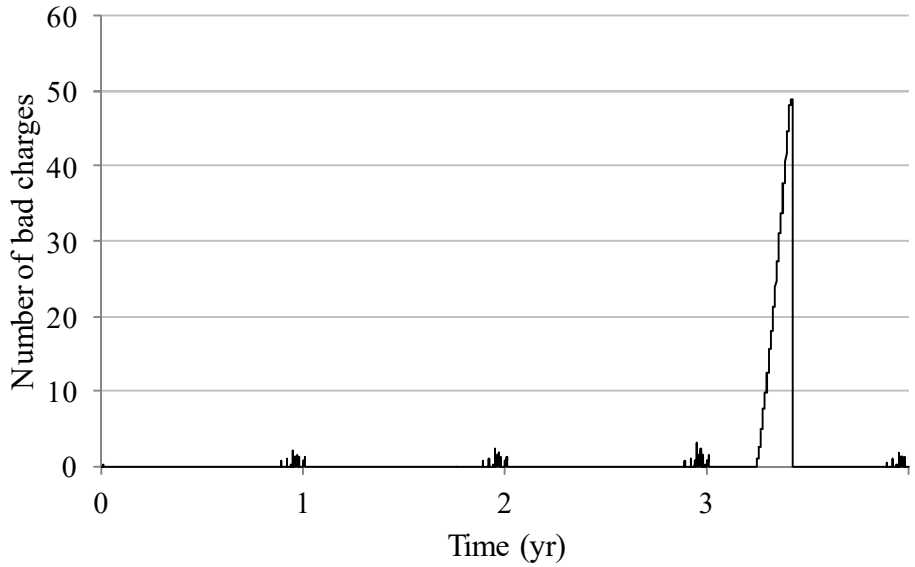

Fig. 8.17. Number of bad charges.

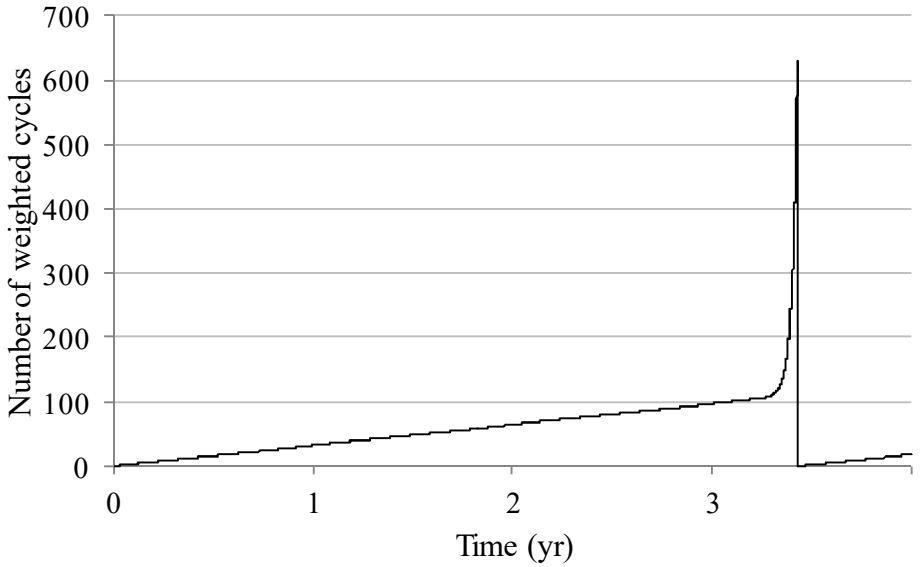

Fig. 8.18. Number of weighted cycles.